Statistics of BY Draconis Chromospheric Variable Stars

Deepak Chahal[1,2]⋆, Richard de Grijs[1,2], Devika Kamath[1,2] and Xiaodian Chen[3]

[1]*School of Mathematical and Physical Sciences, Macquarie University, Balaclava Road, Sydney, NSW 2109, Australia*
[2]*Research Centre for Astronomy, Astrophysics and Astrophotonics, Macquarie University, Balaclava Road, Sydney, NSW 2109, Australia*
[3]*CAS Key Laboratory of Optical Astronomy, National Astronomical Observatories, Chinese Academy of Sciences, Beijing 100101, China*

ABSTRACT

We present an extensive catalogue of BY Draconis (BY Dra)-type variables and their stellar parameters. BY Dra are main-sequence FGKM-type stars. They exhibit inhomogeneous starspots and bright faculae in their photospheres. These features are caused by stellar magnetic fields, which are carried along with the stellar disc through rotation and which produce gradual modulations in their light curves (LCs). Our main objective is to characterise the properties of BY Dra variables over a wide range of stellar masses, temperatures and rotation periods. A recent study categorised 84,697 BY Dra variables from Data Release 2 of the Zwicky Transient Facility based on their LCs. We have collected additional photometric data from multiple surveys and performed broad-band spectral energy distribution fits to estimate stellar parameters. We found that more than half of our sample objects are of K spectral type, covering an extensive range of stellar parameters in the low-mass regime (0.1–1.3 M$_\odot$). Compared with previous studies, most of the sources in our catalogue are rapid rotators, and so most of them must be young stars for which a spin-down has not yet occurred. We subdivided our catalogue based on convection zone depth and found that the photospheric activity index, $S_{\rm ph}$, is lower for higher effective temperatures, i.e., for thinner convective envelopes. We observe a broad range of photospheric magnetic activity for different spectral classes owing to the presence of stellar populations of different ages. We found a higher magnetically active fraction for K- than M-type stars.

Key words: stars: main sequence — stars: rotational variables: chromospheric variables: BY Dra — stars: magnetic field: stellar activity: starspots — stars: stellar rotation — catalogues — surveys

1 INTRODUCTION

In the solar atmosphere, the layers of plasma located above the stellar photosphere exhibit temperature inversion. The temperature increases to $\sim 10^4$ K in the chromosphere, and it peaks at $\sim 10^6$ K in the corona. This heating of the solar atmosphere to such high temperatures is owing to the dissipation of energy carried by magneto-hydrodynamic waves and/or from reconnection of stressed magnetic field lines. The exact physics governing this situation is not yet fully understood. Magnetic fields generated through the solar dynamo process control the structure of the Sun's atmosphere. This leads to phenomena such as large and rapidly evolving starspots (cooler regions where convection is suppressed by magnetic field lines) in the photosphere, strong emission lines from the chromosphere, prominent flares or superflares (sudden releases of magnetic energy) from the corona, etc. (de Grijs & Kamath 2021). Hence, both photospheric magnetic activity (originating in the presence of starspots and bright faculae) and chromospheric magnetic activity (originating in chromospheric emission lines) are indicators of stellar magnetic activity in general.

Stellar magnetic activity is likely triggered by the interplay of rotation and turbulent convection at the stellar surface. Stellar rotation plays an important role in the dynamo efficiency and affects a star's magnetic activity. With increasing age, the loss of angular momentum

induced by magnetised winds and structural variations leads to a rotational spin-down and, hence, it reduces the dynamo efficiency, in turn leading to reduced magnetic activity (Parker 1955; Skumanich 1972). Therefore, we expect young, rapidly rotating late-type stars to exhibit significant magnetic activity. There exist strong correlations among stellar activity and rotation period (Hall 2008; de Grijs & Kamath 2021). Magnetic activity is closely linked to variations in the stellar magnetic field, and it is therefore connected to the structure of the stellar subsurface zone, stellar rotation and the regeneration of the magnetic field through self-sustaining dynamo activity.

These regenerated magnetic field lines produce inhomogeneously distributed dark spots and bright faculae in the stellar photosphere. These features move across the stellar disc through rotation, giving rise to a gradual modulation of the star's luminosity. Such stars are generally referred to as rotational modulators or rotational variables. Fitting a rotational variable's light curves (LCs) with a multiple-order Fourier function allows us to infer its rotation period, which is the key parameter required to explain the stellar activity. The rotation periods of thousands of main-sequence rotational variables have been obtained from *Kepler* observations (Reinhold et al. 2013; McQuillan et al. 2014; Reinhold & Hekker 2020). The amplitude of the LC fluctuations can be used as a proxy of their photospheric magnetic activity (Mathur et al. 2014; Salabert et al. 2016). Larger LC amplitudes imply more significant magnetic activity, i.e., larger fractions or sizes of starspots on a star's surface.

A special class of rotational variables that show strong emission

⋆ E-mail: deepakchahal294@gmail.com

lines in their chromospheres are BY Draconis (BY Dra) variables. BY Dra stars are low-mass main-sequence stars which exhibit low variability amplitudes with periods of a few days; Ca II H and K (and often hydrogen) emission lines are usually present in their spectra (Bopp & Fekel 1977). The variability amplitude of BY Dra, caused by spots and faculae, can reach on the order of several tenths of a magnitude for the most active objects, but it may only be on the order of milli-magnitudes for solar-type stars. Recent observations obtained by the *Kepler Space Telescope* (Reinhold et al. 2013; Mc-Quillan et al. 2014; Reinhold & Hekker 2020), the Zwicky Transient Facility (ZTF; Chen et al. 2020) and the Large Sky Area Multi-Object Fibre Spectroscopic Telescope (LAMOST) Medium-Resolution Survey (Zhang et al. 2019) have provided large numbers of high-quality photometric (with precisions as good as 0.01 mag) and spectroscopic time-series observations of rotational modulators. Lanzafame et al. (2018) presented a catalogue of 147,535 BY Dra candidates, including their rotation periods and modulation amplitudes.

The exact mechanism which drives the stellar dynamo process—and, hence, regeneration of the magnetic field in rotational variables—is not yet properly understood. Therefore, understanding the relationship between stellar rotation and tracers of magnetic activity is important to understand the physics of the stellar dynamo. In addition, it is not yet clear either how the magnetic activity varies across a range of stellar rotation rates, masses and ages. Moreover, it is still uncertain how different the stellar dynamo process is from the solar dynamo's. Therefore, a comparison study with Sun-like active stars offers significant promise to constrain the stellar dynamo process. Statistical studies based on large data sets are still too few to be useful to gain a full understanding of the rotation–activity–age and activity–brightness–age relationships. More precise observations and estimates are required to construct a 'chromospheric Hertzsprung–Russell (HR) diagram'. The latter can be used to show where magnetically active stars are present and how activity varies across the HR diagram.

Using the large ZTF database of BY Dra candidates, we aim to address and quantify stellar magnetic activity across a wide range of stellar masses and rotation periods. Our catalogue (Chen et al. 2020) contains stars of multiple spectral types, ranging from F- to M-type. We have investigated and characterised the physical properties of the BY Dra variables using a combination of LCs and photometric data from multiple surveys. Here we present an extensive catalogue of 78,954 BY Dra candidates with their stellar parameters (effective temperature, radius, luminosity, mass), rotation period and photospheric magnetic index in both the g and r bands. In Section 2, we focus on the catalogue of ZTF BY Dra candidates. That section contains information about the photometric data we adopted from multiple surveys and our further analysis. In Section 3, we discuss the broad-band spectral energy distribution (SED) fitting process we applied and the derived stellar parameters. All photometric data and the derived stellar parameters are included in Tables 1 and 2, respectively. In Section 4, we perform a statistical analysis of the rotation periods and the photospheric magnetic index, S_{ph}. We discuss the relationships between multiple stellar parameters derived from our SED fitting with the S_{ph} index and rotation period for different spectral types. Finally, Section 5 summarises our results.

2 OBSERVATIONS AND DATA ANALYSIS

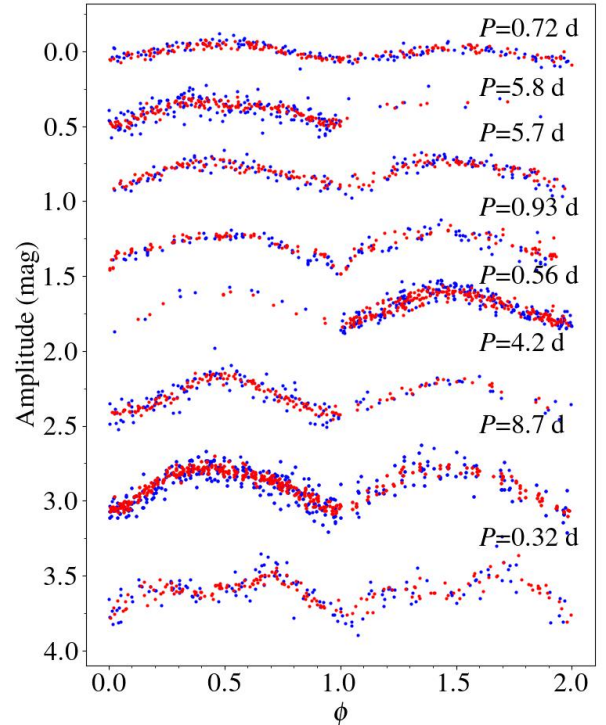In this section, we present the target sample used in this study.

Figure 1. Example LCs of BY Dra variables. The blue and red points represent LCs in the g and r bands, respectively. From top to bottom, the variability amplitude increases; rotation periods are labelled for the respective LCs.

2.1 Target Sample

Our initial target sample is drawn from the ZTF data. The ZTF is an optical time-domain survey undertaken with the 7-inch Oschin–Schmidt telescope at Palomar Observatory (Masci et al. 2019). It is equipped with a 47 deg^2 field of view, which can scan the entire visible northern sky in one night to median depths of $g \sim 20.8$ mag and $r \sim 20.6$ mag.

We adopted the data set from Chen et al. (2020), who used ZTF Data Release 2 (DR2), to search for and classify different types of variable stars. ZTF DR2 contains data acquired between 2018 March and 2019 June, a timespan of ~470 days. Photometric data are available in the g and r bands, obtained with uniform exposure times of 30 s per snapshot observation. The search for periodic variables was done using Lomb–Scargle periodograms (Lomb 1976; Scargle 1982), while the classification was carried out using the DBSCAN method (see Chen et al. 2020, and references therein) based on the distribution of periods, LC parameters and luminosities. Chen et al. (2020) classified 781,602 periodic variables into δ Scuti, EW- and EA-type eclipsing binaries, fundamental-mode (RRab) and first-overtone (RRc) RR Lyrae, classical and Type II Cepheids, semi-regular (SR) variables, Miras and rotational variables, including BY Draconis (BY Dra) and RS Canum Venaticorum (RS CVn) objects.

2.1.1 Classification of Rotational Variables

To estimate the physical parameters associated with the LCs such as the rotation periods and variability amplitudes, Chen et al. (2020) fitted the LCs with a fourth-order Fourier function. Sources with poor LC fits were excluded by optimisation of the R^2 goodness-of-fit parameter, i.e., they removed sources with $R_g^2 < 0.4$ and $R_r^2 < 0.4$. Rotational variables such as RS CVn and BY Dra exhibit periodic
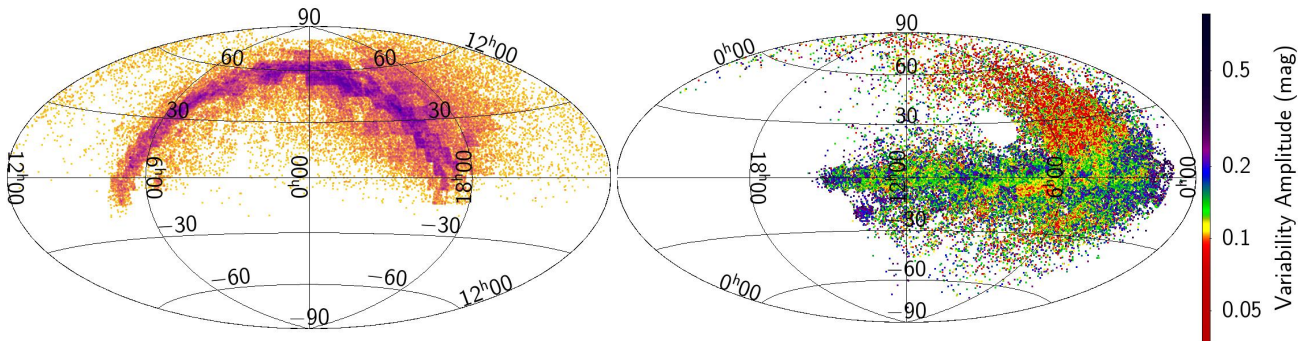
Figure 2. Distribution (left: equatorial coordinates; right: Galactic coordinates) of our sample of 78,954 ZTF BY Dra variables. The map on the right is colour-coded based on variability amplitude.

but non-characteristic LCs (see Figure 1). BY Dra variables exhibit out-of-eclipse LC distortions arising from the rotation of spotted regions, which leads to slow changes in their mean brightness. We have found mean brightness variations in our data on the order of 0.12 mag and 0.10 mag in the *g* and *r* bands, respectively. A few BY Dra example LCs in the *g* and *r* bands are shown in Figure 1. The LCs in both bands look similar. However, in most cases their overall shapes are not symmetric about either phase $\phi = 0.5$ or $\phi = 1.5$. These variables have small variability amplitudes compared with RR Lyrae, Cepheids or eclipsing binary systems; their rotation periods range from a fraction of a day to well over 100 days. BY Dra variables are generally late-type, main-sequence dwarf stars exhibiting enhanced magnetic activity. Chen et al. (2020) observed flaring features in several BY Dra LCs, but those data points were σ clipped prior to LC fitting.

The classification by Chen et al. (2020) based on ZTF DR2 resulted in 84,697 and 81,293 BY Dra and RS CVn stars with purities of 94.6 per cent and 87.2 per cent, respectively. RS CVn are more evolved active stars. RS CVn and BY Dra objects exhibit similar rotation periods, although their luminosities differ significantly, with BY Dra being fainter. Our knowledge of stellar chromospheric activity will benefit greatly from a careful statistical analysis of these rotational variables. In this paper, we focus on the sample of 84,697 BY Dra variables. The full categorised ZTF catalogue is available online.[1] Based on a careful examination of the number density distribution of periodic variable candidates, Chen et al. (2020) imposed a cut-off at a period of 20 days, which seems a natural cut-off for BY Dra variables. This cut-off also removed distant semi-regular variables which may have been misclassified as BY Dra variables, since it is difficult to distinguish between the two types of variables if *Gaia* parallaxes are insufficiently accurate.

We have further refined our target sample by cross-matching our ZTF sample with the *Gaia* early DR3 (EDR3; Gaia Collaboration et al. 2021) catalogue. Stassun & Torres (2021) recently reported that a renormalised unit weight error (RUWE) goodness-of-fit statistic $\gtrsim$ 1.4 indicates likely unreliable astrometry. Objects with high RUWE values could be unresolved binary stars or tight astrometric binaries. Therefore, we have ensured that all stars in our catalogue have RUWE < 1.4 and are thus characterised by reliable *Gaia* parallaxes (as well as the corresponding Bailer-Jones geometric distances, see below; Bailer-Jones et al. 2021)). This left a target sample of 78,954 sources.

The distribution of the 78,954 BY Dra variables in the northern hemisphere is shown in Figure 2. This distribution shows that the majority of our stars are located in the Galactic disc, since ZTF has a higher cadence in the Galactic plane ($\pm 7°$). This is different from the *Kepler* sample, and so our results may indeed differ compared with work resulting from *Kepler* data. Our sample also consists of stars covering a much wider age range. Moreover, the sample's distribution outside the Galactic disc is confined to the solar neighbourhood. The map in Figure 2 (right) shows that the majority of stars in the solar neighbourhood have lower variability amplitudes (shown with red colours in Figure 2), possibly because of our ability to detect fainter magnitude variations at close proximity compared with more distant regimes.

2.2 Photometric Data

To estimate the stellar properties of our target sources we used photometric data covering the optical, near- and mid-infrared wavelength ranges. We found good cross-matches with *Gaia* EDR3 (Gaia Collaboration et al. 2021) for 78,954 sources within a tolerance radius of 1 arcsec. Cross-matching was done using the CDS (Centre de données astronomiques) X-match[2] tool. *Gaia* EDR3 contains updated astrometry and broad-band photometry in the G, G_{BP} and G_{RP} bands. We have used Bailer-Jones et al. (2021) distances—which were estimated using a probabilistic approach—for our follow-up analysis. We had already filtered out unreliable distances by removing sources with RUWE $\geq$ 1.4.

To include photometric data from other surveys, we also cross-matched our sample with the infrared AllWISE catalogue (Cutri et al. 2021) and the Two Micron All-Sky Survey (2MASS) All-Sky Catalog of Point Sources (Cutri et al. 2003). The 2MASS survey scanned the entire sky uniformly in three near-infrared bands (J, H, K). AllWISE combines data from the Wide-field Infrared Survey Explorer (WISE; Wright et al. 2010) and Near-Earth Objects WISE (NEOWISE; Mainzer et al. 2011) surveys to provide the currently most comprehensive view of the mid-infrared sky in four passbands ($W1, W2, W3, W4$). Our cross-matching with the ZTF BY Dra sample resulted in 81,479 and 64,835 sources from the 2MASS and AllWISE surveys, respectively.

The photometric uncertainties in a few of our passbands are rather large compared with the mean amplitude of variability, i.e., they exceed the mean variability amplitude of 0.1 mag in the *r* band. We applied 2σ clipping to remove all photometric data with uncertainties greater than 0.1 mag (~2–3 per cent of our objects). Similarly, for

[1] http://variables.cn:88/ztf/
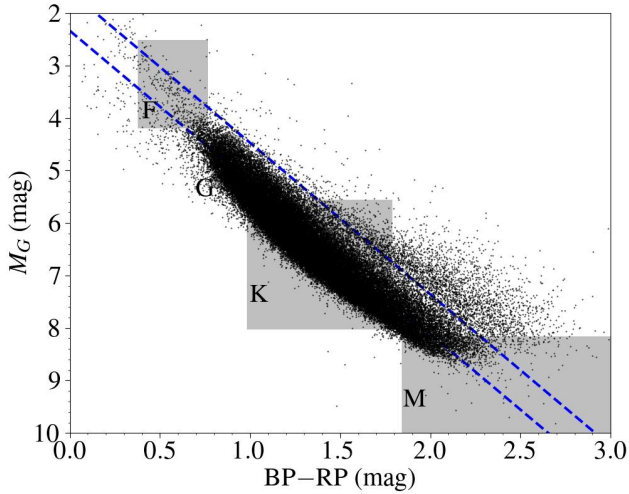
[2] http://cdsxmatch.u-strasbg.fr/

Figure 3. *Gaia* absolute *G*-band magnitude versus ($G_{BP} - G_{RP}$) diagram. Grey regions delineate the F, G, K and M spectral types (Pecaut & Mamajek 2013). The blue dashed lines represents the means in our colour bins; equal-mass (equal-luminosity) binary systems are located 0.753 mag above the mean single-star isochrone.

the parallaxes and *Gaia* distances, all sources with fractional uncertainties greater than 2σ were removed. We corrected for extinction in multiple bands using the 3D map of dust reddening of Green et al. (2019), combined with the Galactic extinction law (Wang & Chen 2019). The 2σ-clipped and extinction-corrected data are included in Table 1, which contains source co-ordinates, *Gaia* astrometry, multipassband photometry, rotation periods and variability amplitudes. The entire table is available electronically in the online journal. This photometry is used in our SED fitting, which is discussed in Section 3.

2.3 Colour–Magnitude Relations

To be able to understand the evolutionary sequence of BY Dra variables, we show the relevant *Gaia* colour–absolute magnitude diagram in Figure 3. We compared our colours with the empirically calibrated main-sequence tables of Pecaut & Mamajek (2013). We found that all of our ZTF sources fall within the F-to-M spectral-type range, as shown in Figure 3. That figure shows that most of our sources overlap with the main-sequence regime (shown as grey boxes), except for the bifurcated sources at fainter magnitudes.

To understand this bifurcation, we compared our ZTF sample with the *Kepler* catalogue of rotational modulators (McQuillan et al. 2014; Reinhold & Hekker 2020). Very few *Kepler* sources lie along the bifurcation observed for our sample. Since previous studies have shown that most BY Dra sources also have a binary companion (for a recent review, see de Grijs & Kamath 2021), we conclude that this bifurcation is most likely caused by the presence of binary systems in our sample, especially K- and M-type binaries. Since we do not have radial-velocity or spectroscopic data, it is beyond the scope of this paper to study the physical properties of these binaries. To classify the bifurcated sources we eliminated any nearly equal-mass binaries which are typically located 0.753 mag above the single-star main sequence (as shown by the blue dashed lines in Figure 3).

3 STELLAR PARAMETER ESTIMATES

The colour–magnitude diagram offers a good handle on the stellar parameters. However, better estimates of the stellar effective temperatures can be obtained through SED fitting. In this section, we present the stellar parameters derived from our photometry (see Section 2). We constructed the stellar SEDs and performed broad-band SED fitting. The final stellar parameters result from the specific SED model which best fits the observations, based on χ^2 minimisation.

3.1 Estimating Temperature, Luminosity and Radius based on SED Fitting

The SEDs were constructed using the available photometric data from the ZTF, *Gaia* EDR3, 2MASS and AllWISE surveys. We used the Virtual Observatory SED Analyzer[3] (VOSA; Bayo et al. 2008) for our broad-band SED fitting. VOSA generates synthetic photometry from theoretical spectra, which are then compared with the observed data and a statistical (minimum reduced-χ^2) test is performed to determine which model best reproduces the observed data. We used the BT-Settl (CIFIST) stellar atmosphere model (Allard et al. 2011). This model contains a grid of theoretical spectra, which is valid across the entire parameter range of interest here and uses the Caffau et al. (2011) solar abundances.

The results of the broad-band SED fits are included in Table 2. Table 2 can be accessed electronically in its entirety in the online journal. The Table 2 contains the source coordinates and stellar parameters such as $T_{\rm eff}$, $\log g$, luminosity, radius, mass, age and the photospheric magnetic index ($S_{\rm ph}$). We present a few example SED fits in Figure 4. That figure shows a number of best-fitting SEDs characterised by different reduced-χ^2 values. It is evident that the sample SEDs with large reduced-χ^2 values nevertheless fit most of the data points well. Therefore, we only removed sources for which we have fewer than seven photometric data points since such sparse wavelength coverage results in unacceptably poor SED fits. We note that many SED fits show a slight dip in the ZTF *r* band (central wavelength $\lambda = 6250$ Å), as can be seen in Figure 4. This dip might be related to the presence of an Hα feature.

We probed $T_{\rm eff} \in [2800 - 7000]$ K in steps of 100 K and allowed $\log g$ to vary between 3.5 and 5.0, i.e., covering the typical range of cool and low-mass stars (including FGKM spectral types; see the colour–magnitude diagram in Section 2) (Kubiak et al. 2021). However, note that the SED fitting procedure is mostly insensitive to $\log g$. Therefore, the main parameter constrained by our SED fitting is $T_{\rm eff}$. The luminosities were derived from the best-fitting observed flux and the radius were estimated from the Stefan–Boltzmann equation (for more details, see Bayo et al. 2008). Since the SED analysis is not sensitive to $\log g$, the resulting masses obtained from using $\log g$ are not well-determined. The $T_{\rm eff}$ values imply that more than half of our stars are of K spectral type, with the respective fractions progressively decreasing for G, M and F types (see Table 3).

The effective temperature, $T_{\rm eff}$, controls the width of the convective envelope in a star. As $T_{\rm eff}$ increases, the convective envelope becomes thinner. The depth of the convective envelope increases towards lower effective temperatures and masses; below ~ 0.3 M$_\odot$, stars are fully convective. The presence of a convective envelope plays a significant role in the regeneration of magnetic fields through dynamo physics (de Grijs & Kamath 2021, and references therein). Hence, stars with larger convective envelopes will be more magnetically active. Our

---

[3] http://svo2.cab.inta-csic.es/theory/vosa/

Table 1. LC data from Chen et al. (2020) combined with photometric data of BY Dra variable candidates from multiple surveys.

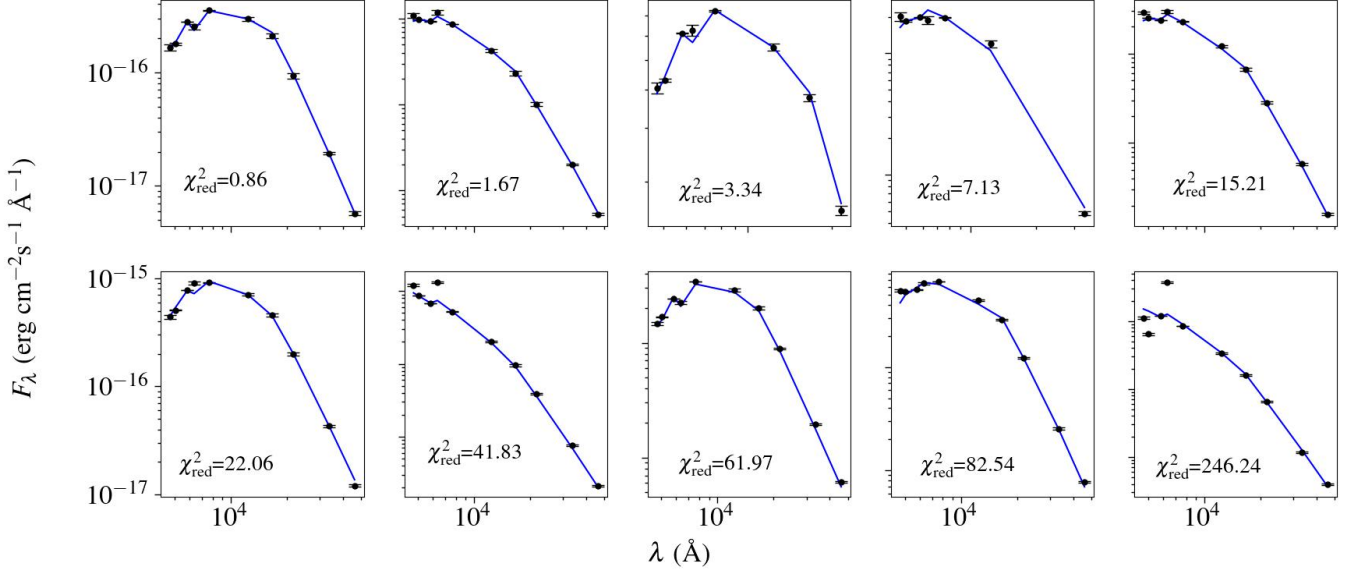| ID	RA (J2000) (deg)	Dec (J2000) (deg)	Parallax (mas)	Distance (pc)	$\langle g \rangle$ (mag)	$\langle r \rangle$ (mag)	$\langle G \rangle$ (mag)	$\langle BP \rangle$ (mag)	$\langle RP \rangle$ (mag)	$\langle J \rangle$ (mag)	$\langle H \rangle$ (mag)	$\langle K \rangle$ (mag)	$\langle W1 \rangle$ (mag)	$\langle W2 \rangle$ (mag)	...	Period (days)	Amp_g (mag)	Amp_r (mag)	...
ZTFJ000000.13+620605.8	0.00056	62.10163	1.58	636.77	16.79	15.73	15.77	16.56	14.95	13.83	13.24	13.06	—	—	...	1.945	0.113	0.078	...
ZTFJ000002.20+480720.8	0.00918	48.12246	1.96	510.07	16.87	15.81	15.88	16.60	15.06	14.04	13.41	13.25	13.18	13.19	...	0.381	0.107	0.093	...
ZTFJ000003.23+543605.4	0.01347	54.60151	1.15	846.92	17.20	16.22	16.33	17.03	15.52	14.45	13.73	13.73	13.56	13.63	...	0.786	0.166	0.112	...
ZTFJ000003.76+532917.1	0.01568	53.48811	0.89	1116.84	15.84	15.32	15.35	15.73	14.79	14.20	13.74	13.59	13.66	13.66	...	0.592	0.164	0.159	...
ZTFJ000004.34+522031.5	0.01809	52.34209	0.92	1078.8	17.04	16.28	16.41	16.94	15.73	14.98	14.32	14.26	14.16	14.22	...	4.083	0.087	0.095	...
...	...	...			...	...	...	...	...	...	...	...	...	...	...	...	...	...	...
...	...	...			...	...	...	...	...	...	...	...	...	...	...	...	...	...	...

Figure 4. Example SEDs of BY Dra candidates. The black filled circles with error bars are the observed photometric data points, whereas the blue line represents the best-fitting BT-Settl (CIFIST) model (see the text).

Table 2. Stellar Parameters of our sample BY Dra variable candidates

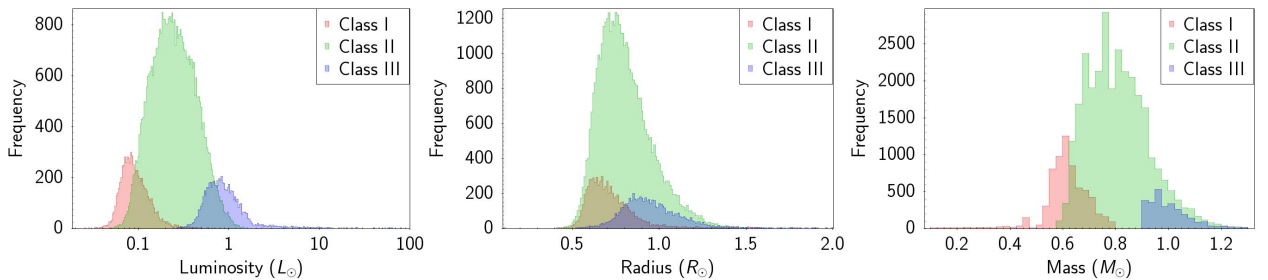| ID	RA (J2000) (deg)	Dec (J2000) (deg)	...	T_{eff} (K)	$\log g$ (cm s^{-2})	χ^2_{red}	Luminosity ($L_\odot$)	$\pm$ ($L_\odot$)	Radius ($R_\odot$)	$\pm$ ($R_\odot$)	Mass ($M_\odot$)	...	Age (Gyr)	...	$S_{ph,g}$ (ppm)	$S_{ph,r}$ (ppm)
ZTFJ000000.13+620605.8	0.00056	62.10163	...	4200	4.5	9.82	0.215	0.014	0.87	0.025	0.8	...	0.03	...	2121	1406
ZTFJ000002.20+480720.8	0.00918	48.12246	...	4300	5	8.65	0.117	0.005	0.61	0.01	—	...	—	...	—	—
ZTFJ000003.23+543605.4	0.01347	54.60151	...	4200	2.5	5.15	0.224	0.018	0.90	0.03	0.81	...	0.028	...	3104	2324
ZTFJ000003.76+532917.1	0.01568	53.48811	...	5400	4.5	6.01	0.694	0.04	0.95	0.02	0.91	...	0.037	...	3056	2847
ZTFJ000003.34+522031.5	0.01809	52.34209	...	4700	3.5	2.95	0.278	0.032	0.795	0.043	0.78	...	0.05	...	2037	1438
...	...	...	...	...	...	...	...	...	...	...	...	...	...	...	...	...
...	...	...	...	...	...	...	...	...	...	...	...	...	...	...	...	...

Figure 5. Histogram of stellar parameters derived from the broad-band SED fits. (right) Luminosities (in units of $L_\odot$); (middle) radii (in units of $R_\odot$); (left) masses (in units of $M_\odot$).

Table 3. Classification of BY Dra candidates based on their convection zone depth.

Spectral Type	No. of Sources	Fraction
Class I ($\leqslant$ 3900 K)	10,336	12 per cent
Class II (3900–5400 K)	47,119	56 per cent
Class III ($\geqslant$ 5400 K)	6879	8 per cent

sample, which contains predominantly K-type stars, is dominated by convection. The fraction of fainter, M-type stars is smaller. The latter are fully convective. The lower fraction of M-type stars is owing to the fact that our observations are limited by instrument capabilities. The fraction of F-type stars is just 2 per cent. This is not unexpected, since these stars have very thin outer convection zones.

To properly understand our full data set of 78,954 objects, we classified all sources into three classes based on the depths of their convective zones (see van Saders & Pinsonneault 2012). Figure 1 of van Saders & Pinsonneault (2012) shows the variation of the convective zone depth with $T_{\rm eff}$. It shows steep slopes for lower and higher $T_{\rm eff}$ values and a roughly constant plateau in between. The statistics of our classification are summarised in Table 3. Class I objects have $T_{\rm eff} \leqslant 3900$ K. Here, the depth of the convective zone increases exponentially for progressively lower effective temperatures. Class II objects have $T_{\rm eff}$ between 3900 and 5400 K, a temperature regime where the convective zone depth is approximately constant (within 5–10 per cent). Finally, Class III sources have $T_{\rm eff} \geqslant 5400$ K, where the depth of the convective zone decreases exponentially with increasing effective temperature.
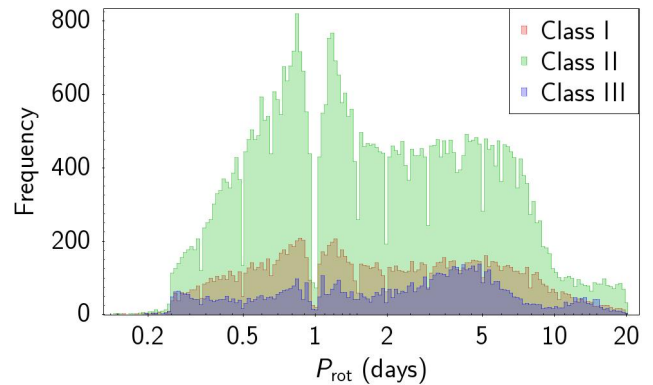
The ranges of luminosities and radii for different classes of objects are shown in Figure 5. This figure shows that there is a significant overlap in radii among the different classes, whereas the luminosities are mostly distinct. Our derived radius and luminosity estimates suggest that most of our sample stars are of F to M spectral types.

3.2 Estimating Masses and Ages from Isochrone Fitting

With increasing age, a star spins down and, hence, its stellar activity decreases (Skumanich 1972). Therefore, information related to masses and ages is important to understand the stellar activity. We estimated our stellar masses and ages by fitting a 'Stellar Parameters Of Tracks with Starspots' (SPOTS) model (Somers et al. 2020). This model contains a grid of solar-metallicity stellar evolutionary tracks and isochrones which include treatment of the structural effects of starspots. The model covers the stellar mass range of 0.1–1.3 $M_\odot$ and a surface covering fraction from 17 to 85 per cent. In this model, stars are evolved from the pre-main-sequence to the red-giant-branch phase.

The mean of the variability amplitude of the ZTF data is approximately 0.14 mag in the g band, which results in a spot fraction of 12 per cent (assuming that the LC variability is entirely caused by starspots). Therefore, for our isochrone fitting we have adopted the model with a spot fraction of 17 per cent, i.e., the SPOT-f017 model. The estimated mass values do not have large errors, but they show clustering owing to the discrete values of $T_{\rm eff}$ contained in the model. Meanwhile, the age estimates from the isochrone fits are subject to large errors, and hence they are unreliable.

Figure 5 shows a histogram of the stellar masses for the different classes of objects, ranging from 0.1 to 1.3 $M_\odot$. The mass distributions are different for the different classes of objects, with only small overlaps. Figure 5 shows that our ZTF catalogue contains sources

Figure 6. Histogram of the rotation periods of our 65,735 BY Dra candidates, where different colours correspond to different classes of objects.

spanning a wide variety of stellar parameters in the low-mass regime, especially for Class II ($T_{\rm eff} \in [3900 - 5400]$ K) objects.

3.3 Rotation Periods

The rotation periods of our sample objects were estimated by Chen et al. (2020), based on fits to their LCs, as discussed in Section 2. We have adopted the latter authors' periods. There is a possibility that some of the rotation periods in our catalogue, particularly those with values near 1 day, might be aliased periods owing to the Earth's rotation. However, Chen et al. (2020) were clearly aware of this potential bias. They attempted to avoid it from occurring as evidenced by, e.g., the distinct dearth of periods near 1 and 0.5 days evident in Figure 6 (and also in other figures in this paper). The rotation periods of ZTF BY Dra objects range from 0.15 days to 61 days. A histogram of the rotation periods for 65,735 BY Dra candidates is shown in Figure 6; the mean of the distribution is 1.86 days. We found that 32 per cent, 62 per cent and 5 per cent of sources have periods of less than one day, between 1 and 10 days, and longer than 10 days, respectively. Hence, a large fraction of our sample objects rotate rapidly compared with the objects in the *Kepler* catalogue of rotational modulators (McQuillan et al. 2014; Reinhold & Hekker 2020). This means that a large fraction of our sample stars are young (probably in the early main-sequence phase) and, hence, the spin-down effect has not yet occurred (Skumanich 1972). The statistics of the rotation periods of our ZTF BY Dra sample agree well with those pertaining to the *Gaia* catalogue of rotational variables, covering late-type dwarfs (Lanzafame et al. 2018).

In Figure 6, we see a clear bimodality at a rotation period of ~2 days, for different classes. This bimodal period distribution at ~2 days has not been observed in previous studies based on *Kepler* data (McQuillan et al. 2014; Reinhold & Hekker 2020; Gordon et al. 2021). The rotation distributions of the different classes show a lack of intermediate-period rotators. A similar conclusion was reached by Reinhold & Hekker (2020). However, we did not find any significant decrease in the variability amplitude at ~2 days. Therefore, its less likely that the bimodality arises from the non-detection of rotation periods because of the temporal increase in bright faculae, which dilutes the starspot effect (Reinhold & Hekker 2020).

3.4 The Photospheric Magnetic Index

LC variability is associated with the rotation of starspots, and thus it can be used as a proxy of stellar activity. Surface magnetic activ-
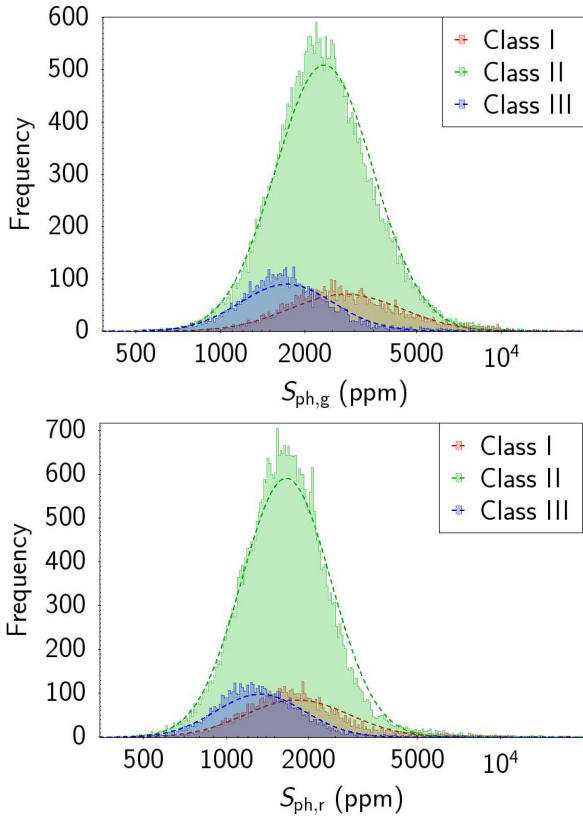
Figure 7. Histograms of the photospheric magnetic index (S_{ph}) in (top) the *g* and (bottom) *r* bands for different classes of objects.

Figure 8. Rotation period versus absolute Wesenheit magnitude ($M_{W_{gr}}$) diagram, colour-coded with the variability amplitude in the *g* band.

ity arises owing to the regeneration of magnetic fields through the dynamo process in the stellar interior, which is linked to the stellar rotational period. By taking into account a star's rotation period, the derived activity index, S_{ph}, can be adopted as a proxy for its magnetic activity (Mathur et al. 2014). The S_{ph} index is defined as the mean value of the standard deviation of the LC estimated over $5P_{rot}$. The measured photospheric magnetic index is only related to magnetism (i.e., starspots) and not to other sources of variability such as stellar oscillations, convective motions or instrumental issues (Mathur et al. 2014). Since this index depends on the angle of inclination of the rotation axis relative to the line of sight, it must be considered a lower limit to the photospheric activity. Salabert et al. (2016) compared the $\langle S_{ph} \rangle$ index with the spectroscopic S index (the usual chromospheric activity index, derived by measuring chromospheric Ca ɪɪ H and K line fluxes) (Wilson 1968) and found a good correlation.

Histograms of the S_{ph} index in both the *g* and *r* bands are shown in Figure 7, where different colours correspond to different classes, as specified in Section 3. We see a clear distinction in the distributions of the different classes, although the distributions are very wide, i.e., spread over a broad range of the activity index (see Figure 7). The means of the S_{ph} histograms in the *g* and *r* bands are 2486 and 1750 ppm (parts per million), respectively. Since the ZTF *r* band is highly sensitive to chromospheric emission from active regions, the amplitude arising from the rotation of starspots is diluted by chromospheric emission in the *r* band.
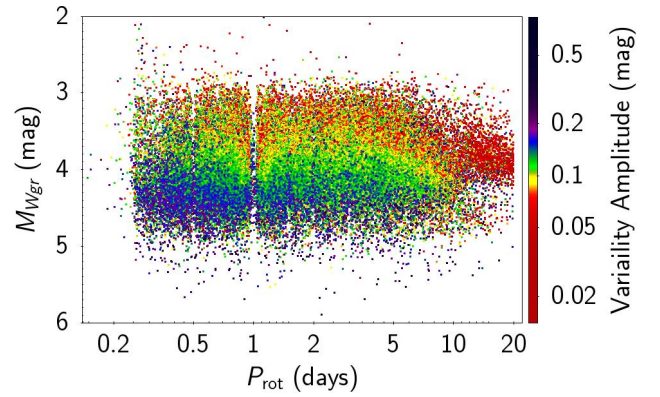
4 DISCUSSION

BY Dra represent a population of magnetically active K–M-type main-sequence stars which show low amplitude variability and strong chromospheric emission. Because of their low-amplitude variability, BY Dra variables have not previously been studied statistically, until the recent study by Lanzafame et al. (2018). We are interested in understanding the stellar properties and evolutionary nature of this class of stars. These low-mass main-sequence stars exhibit low to high magnetic activity in the form of starspots, chromospheric activity, flares, etc. The observed photospheric and chromospheric activity indicators have a similar origin. However, the exact origin of these magnetic events is not yet properly understood.

It has been argued that convection and differential rotation may play a significant role in the generation of stellar magnetic activity. Turbulent convection and differential rotation induce dynamical instabilities and, hence, play a key role in the regeneration of magnetic fields through dynamo activity. Therefore the presence of a convective envelope (which is related to stellar mass), as well as differential rotation, are the key ingredients that induce stellar magnetic activity through the dynamo process. Hence, in this section we explore the mutual dependencies of different stellar parameters such as rotation period, effective temperature, mass, etc. on stellar activity. By virtue of our large catalogue, we have managed to statistically characterise the relationships of these stellar parameters with the photospheric magnetic activity index.

4.1 Period–Luminosity Relation

To investigate the relationships among our photometric data, our objects' rotation periods and their variability amplitudes, we plotted the rotation periods and the ZTF absolute Wesenheit magnitudes (which are a proxy of extinction-free luminosity) in Figure 8. The Wesenheit magnitude was obtained through $m_{W_{gr}} = 3.712\langle r \rangle - 2.712\langle g \rangle$ (Chen et al. 2020). It is evident that sources corresponding to long rotation periods (slow rotators) and high luminosities (absolute magnitudes) have lower variability amplitudes (shown in red in Figure 8) and, hence, relatively lower fractions of starspots. Meanwhile, more rapidly rotating sources exhibit lower luminosities and, hence, higher variability amplitudes (shown in blue in Figure 8), i.e., they have relatively larger fractions of starspots. Therefore, rapidly rotating lower-luminosity stars of late spectral types, i.e., possessing thicker convective envelopes, exhibit higher magnetic activity and, hence, larger fractions of starspots.
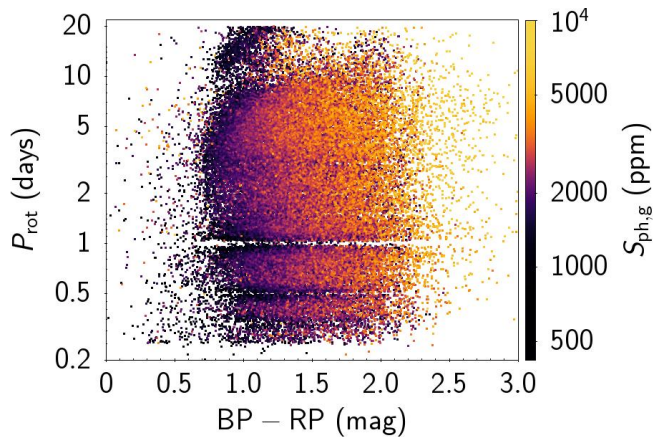
Figure 9. Rotation period versus *Gaia* ($G_{BP} - G_{RP}$) colour diagram, colour-coded with the photospheric magnetic index (S_{ph}) in the *g* band.
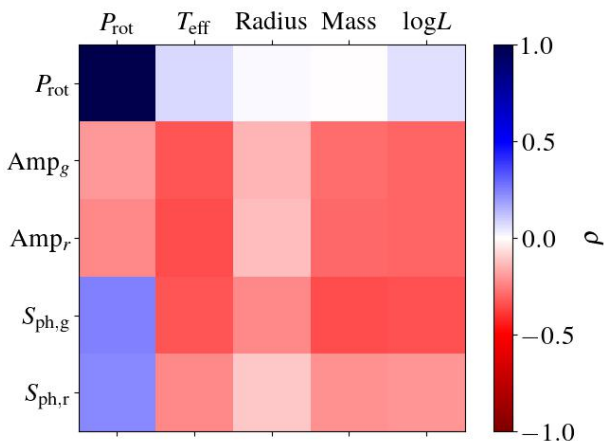

Figure 10. Spearman correlation coefficient (ρ) matrix of stellar parameters (rotation period, T_{eff}, radius, luminosity and mass) and stellar activity (variability amplitude and photospheric magnetic index).

4.2 Period Gap

As highlighted in Section 3, we observe a bimodal distribution at a rotation period of ~2 days. We also observe a bimodal distribution at the period of ~10 days (see Figure 6). The latter bimodal distribution has been found previously in *Kepler* and K2 data (McQuillan et al. 2014; Reinhold & Hekker 2020; Gordon et al. 2021). In order to understand this specific bimodality in detail, in Figure 9 we have plotted the *Gaia* colour–rotation period distribution. In this figure, we observe a small clump, and a gap below it, at a period of ~10 days (see Figure 9, top left). The clump and gap are also visible for a constant Rossby number (~0.5–0.7; see below) in Class II objects: see Figure 11. The gap is prominent for G–K-type stars. It appears to be a continuation of the gap previously observed in *Kepler* and K2 data (McQuillan et al. 2014; Reinhold & Hekker 2020; Gordon et al. 2021). Gordon et al. (2021) found that the gap extends from 15–25 days, whereas the gap in our data occurs at shorter periods and redder colours, as if it were an extension of their gap. Several explanations of the observed bimodality and associated gap have been proposed. McQuillan et al. (2014); Davenport & Covey (2018) suggested that the bimodality may be owing to a bimodal star-formation history, with an older population of stars forming a slowly rotating branch and a more recent burst of star formation corresponding to the rapidly

rotating branch. Independently, (Reinhold & Hekker 2020) suggested that these features may be owing to the non-detection of a range in rotation periods because of a temporary increase in bright faculae and, hence, dilution of the starspot effect.

Gordon et al. (2021) suggested that since the stellar core and envelope are initially not coupled, the envelope slows down because of magnetic braking, while the core may continue to spin rapidly. Magnetic braking results in a spin-down, as the star loses angular momentum through magnetic activity. After a period of time, the core and envelope start to exchange angular momentum. In turn, this counteracts the spin-down, thus resulting in an overdensity of periods below the gap. If this is indeed the case, we should have observed only a low level of activity at the bottom of the period gap, given that the spin-down would have been halted. Although we do see lower activity for F–G-type stars, we also observe a higher level of activity for K–M-type stars at the bottom of the gap (see Figure 9).

Gordon et al. (2021) also suggested that the underdensity within the gap might have been caused by an additional stage of accelerated spin-down immediately following the stalled spin-down phase. This accelerated spin-down could be owing to a temporary increase in stellar magnetic activity. If such an accelerated spin-down could have caused the observed underdensity, then the activity above the period gap should be higher relative to that in the overdense region at the bottom of the gap. However, we do not see enhanced activity. Rather, in Figure 9 we observe stars with a relatively low level of activity above the period gap. Since the photospheric magnetic index is prone to dilution owing to the presence of bright faculae, it tracks the minimum stellar activity. A more detailed analysis using the chromospheric activity index of the period–colour gap will offer greater constraints on the gap's origin.

4.3 Correlation Study

The mutual dependencies among rotation period, stellar activity and stellar parameters are complex and, hence, not yet fully understood. Since we have a large data set of magnetic variables, we have explored correlations among multiple parameters: see Figure 10. We derived the Spearman correlation coefficients (ρ) for different stellar parameters and provide a correlation matrix in Figure 10. However, we obtained low correlation coefficients for most parameter combinations because of the complex interdependencies. Still, negative correlations are discernible between certain stellar parameters (T_{eff}, luminosity and mass) on the one hand and, on the other, the amplitude of variability and photospheric magnetic index (shown in red in Figure 10). This is expected, since with the increase in stellar parameters (i.e., an increase in T_{eff} or mass), the width of the convective envelope decreases and, hence, stellar activity decreases. The stellar radii show a modest anti-correlation with stellar activity.

We expect the stellar activity to increase for rapidly rotating stars. In Figure 10, we see a modest negative correlation of rotation period with variability amplitude, as expected. However, we see a slight positive correlation of rotation period with S_{ph} index, which might be related to how the S_{ph} index is estimated (i.e., from the mean values of the standard deviation over $5P_{rot}$). The poor correlation of rotation period with stellar activity might be because of the relatively narrow range in rotation period covered by our sample, given that 87 per cent of our sources have rotation periods between 0.4 and 9 days. In Figure 10 we also notice the lack of clear correlations between rotation period and certain stellar parameters (T_{eff}, luminosity, radius and mass).
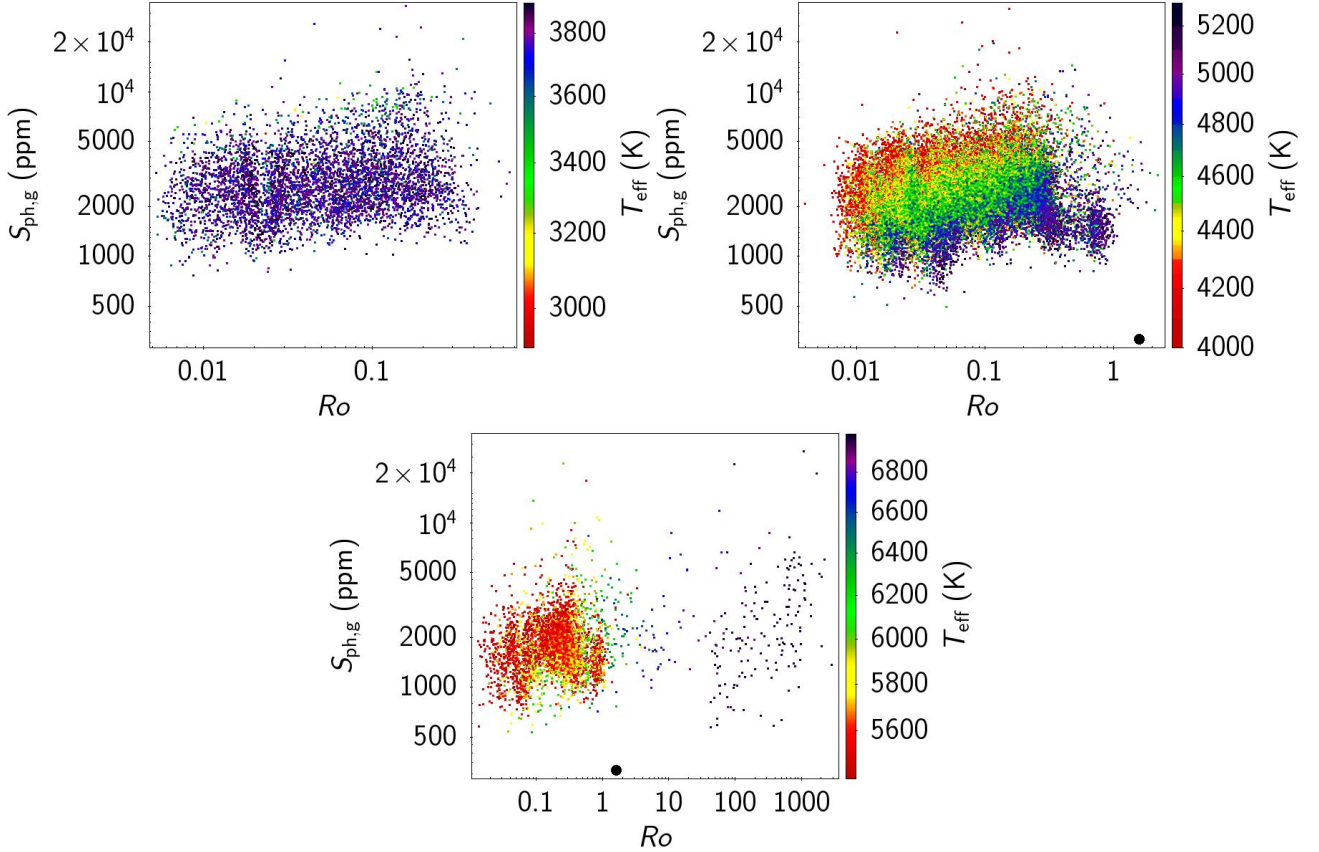
Figure 11. Rossby Number versus $S_{\rm ph}$ index for different classes of objects, with the temperature distribution colour-coded. (Top left) Class I; (top right) Class II; (bottom) Class III. The black point at the bottom is the position of the Sun.

4.4 Rossby number–Activity–Temperature

Stellar chromospheric activity correlates very well with the so-called Rossby number (Noyes et al. 1984), $Ro \equiv P_{\rm rot}/\tau_{\rm c}$, where $\tau_{\rm c}$ is the convective turnover time. The latter is estimated from the analytical equation derived from the parametrised fit as a function of effective temperature (for more details, see Cranmer & Saar 2011). The Rossby number probes the interplay between rotation and convection which is responsible for driving dynamo action. Figure 11 shows the relationships among the Rossby number, $S_{\rm ph}$ index and $T_{\rm eff}$ for the different classes of objects.

Among Class III objects, the width of the convective envelope becomes increasingly thinner, and therefore most of these objects are less active and, hence, have lower $S_{\rm ph}$ values. Few F-type stars (especially, $T_{\rm eff} > 6500$ K) have large Rossby numbers because of very small values of the convective turnover time, derived from the analytical equation by Cranmer & Saar (2011) (can be seen as black data-points in Figure 11). Class II objects show a clear variation with $T_{\rm eff}$; as $T_{\rm eff}$ increases, i.e., as the convective envelope becomes thinner, we see a clear decrease in the $S_{\rm ph}$ index. However, for Class I objects, which are M-type stars, a similar trend with $T_{\rm eff}$ is not so clear, possibly owing to the increasingly thicker envelopes and eventually the absence of a tachocline, resulting in a turbulent dynamo (Strassmeier 2009). The convective envelope in this class of stars is so deep that the resulting dynamo detaches from the surface or loses its connection (as for tachocline stars; Strassmeier 2009).

We see a broad range in stellar activity among Classes I and II. This might be caused by the presence of a wide range of ages

in the different classes. As for age, the rotation period of a star increases, i.e., the star rotates increasingly slowly owing to spin-down. Hence, stellar activity decreases with increasing age. The broad ranges in the photospheric stellar activity also arise because of the more even distribution of starspots across the stellar disc or the presence of starspots away from the line of sight, or both. Hence, we see a decrease in the variability amplitude in the LCs. Therefore, the photospheric magnetic index $S_{\rm ph}$ underestimates the magnetic activity of a star. The Sun's position is shown as the black filled circle in Figure 11. The $S_{\rm ph}$ index of the Sun was taken from Salabert et al. (2016). The Sun belongs to a category of less active stars; all of our sources have activity levels in excess of that of the Sun.

The distribution of Rossby number versus $S_{\rm ph}$ index shows a kink in both Classes I and II (see Figure 11). The kink corresponds to a change in the slope of the distribution from a saturated to a linear dependence of the photometric activity index on Rossby number. This kink corresponds to $Ro \approx 0.2$–0.3 and $S_{\rm ph} \approx 10^4$ ppm, which is in agreement with the kink's locus found by Corsaro et al. (2021) and See et al. (2021). In coronal X-ray emission, Pizzolato et al. (2003); Reiners et al. (2014) found a similarly saturated regime at smaller Rossby numbers and subsequent linear dependence. However, we do not observe a clearly saturated region for smaller Rossby numbers as found by Corsaro et al. (2021). Instead, we see a slight decline of the $S_{\rm ph}$ index for smaller Rossby numbers. Corsaro et al. (2021) and See et al. (2021) explored the flat, saturated region to $Ro = 0.1$, whereas our data reach $Ro = 0.01$. Therefore, we can say that there is slight decline in the saturation limit for very small Rossby numbers. The slope of the decline is steeper for Class I objects, which are highly
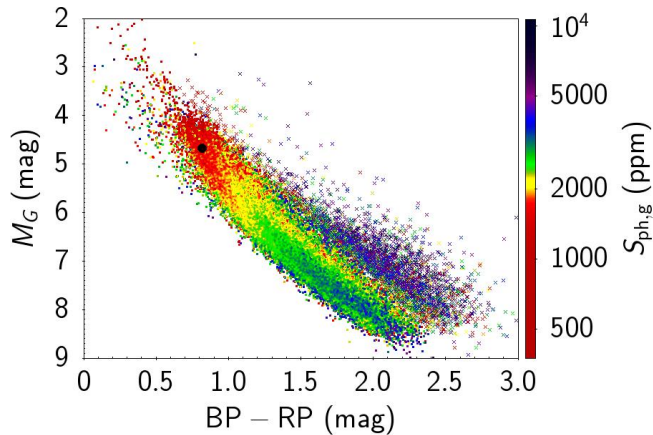
Figure 12. *Gaia* absolute colour–magnitude diagram (CMD), colour-coded with the photospheric magnetic index (S_{ph}) in the g band. The black point is the position of the Sun in the *Gaia* CMD (Casagrande & VandenBerg 2018). Cross sign are the probable binary systems classified in Section 2
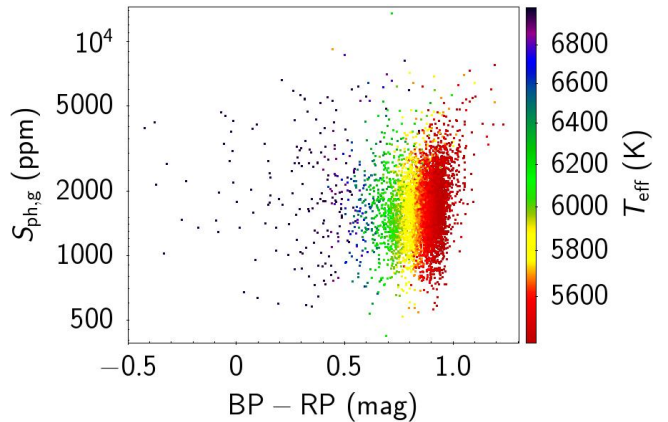

Figure 13. *Gaia* ($G_{\text{BP}} - G_{\text{RP}}$) colour versus photospheric magnetic index diagram for F- and G-type stars, with the temperature distribution colour-coded.

active, and decreases for the other classes. This decline might be caused by bright faculae partially cancelling out dark spots, resulting in a reduction in the overall variability amplitude. Alternatively, this trend might have originated from the way the S_{ph} index is estimated (i.e., from the mean values of the standard deviation over $5P_{\text{rot}}$), because we did not find any such decline in variability amplitude for lower Rossby numbers.

We also found that all categories of stars (i.e., slow, intermediate and rapid rotators) exhibit a wide range of stellar activity. To fully understand the context, age is an important parameter that must be taken into consideration. With increasing age, stars lose angular momentum and spin down, which leads to a decrease in stellar activity. Age estimates from isochrone fits have large associated errors. We will be able to constrain rotation periods, stellar parameters and magnetic activity more optimally once accurate age estimates have been obtained. We will explore ages in a future paper.

4.5 Chromospheric Hertzsprung–Russell diagrams

We have some evidence that stellar magnetic activity is generated through a process akin to that governing the solar dynamo. Yet, it is still questionable whether or not the stellar dynamo which generates stellar magnetic activity is similar to that operating in the Sun. Therefore, studying stellar magnetic activity with reference to solar activity could help in understanding how different the stellar dynamo process may be from the solar dynamo for different classes of stars.

We show the *Gaia* colour–absolute magnitude diagram of BY Dra candidates, including the density distribution of the S_{ph} index, in Figure 12. It shows that as the temperature increases, the convective envelope becomes thinner and, hence, the S_{ph} index decreases. Salabert et al. (2016) estimated the Sun's maximum S_{ph} index at 314.5 ppm, which is well below the S_{ph} index measured for the majority of the stars in our catalogue. As we have already noted, our catalogue contains very young stars (since most are rapidly rotating), and therefore we observe higher activity levels for our sample stars compared with the Sun. The Sun belongs to a class of low-to-moderately magnetically active stars. This result is also in agreement with Reinhold et al. (2020), who compared 369 solar-like stars with the Sun.

Using our large catalogue of chromospherically active variables we constructed a 'chromospheric HR diagram', which shows where Sun-like chromospheres are expected to be found. Figure 12 shows

that F- and late-G-type stars exhibit very low levels of stellar activity and that the activity increases towards K–M-type stars. By virtue of our large database, we conclude that most of the rotationally and magnetically active main-sequence stars in our sample are of later spectral type than F6V. We also found that late-K-type stars are most magnetically active, even more so than M-type stars. The cross signs in Figure 12 show that the probable binary systems are highly active stars (visible in blue above the main sequence region at the bottom of Figure 12), which is expected since the presence of a companion increases the magnetic activity in the primary star (de Grijs & Kamath 2021).

4.6 The Putative Vaughan–Preston Gap

An apparent dearth of F- and G-type stars of intermediate activity was discovered by Vaughan & Preston (1980) based on a sample of 486 stars. We also investigated this putative 'Vaughan–Preston gap' for our sample of active F- and G-type stars. We present the S_{ph} index versus *Gaia* colour diagram in Figure 13 to investigate the dearth of intermediate-activity stars. Figure 13 shows clear signatures of the presence of stars of intermediate activity, and we observe a good spread in the magnetic activity (500–5000 ppm) of F- and G-type stars. We do not even observe a bimodal distribution in the photospheric activity index, as was seen by Boro Saikia et al. (2018). By virtue of our large data set, we conclude that the putative Vaughan–Preston gap may have been caused by a lack of data from stars of intermediate activity and, hence, this gap might not be a true manifestation of stellar dynamo activity.

5 CONCLUSIONS

In this paper, we have compiled a catalogue of low-mass main-sequence stars which exhibit varying levels of stellar magnetic activity. We present a large catalogue of 78,954 BY Dra candidates, including their photometric measurements, rotation periods, variability amplitudes, etc. This large catalogue has aided us in understanding the evolutionary nature of BY Dra variables. Through broad-band SED fitting, we estimated their stellar parameters, including the effective temperatures, radii, luminosities, masses, etc. We found that more than half of our sample objects are K-type stars, and the respective fraction decreases for G (12 per cent), M (8 per cent) and F (2

per cent) types. The ZTF catalogue of BY Dra candidates contains an extensive range of stellar parameters in the low-mass regime (0.1–1.3 $M_\odot$).

Our ZTF catalogue contains rapidly rotating stars (94 per cent have rotation periods $\leqslant 10$ days) compared with the *Kepler* catalogue of rotational modulators (see Reinhold & Hekker 2020; McQuillan et al. 2014). This high rotation rate might have resulted because most of our sample stars are young (probably in the early phases of the main sequence) and, hence, the inevitable spin-down might not yet have occurred (Skumanich 1972). To investigate the dependence of stellar magnetic activity, we have studied their correlation with multiple stellar parameters. We observed a negative correlation between the stellar activity (variability amplitude and S_{ph} index) and a number of stellar parameters (T_{eff}, luminosity and mass), i.e., the activity decreases for hotter stars. This is expected, since with increasing T_{eff} or mass, the convective envelope becomes thinner, hence stellar activity decreases. We also noted a negative correlation between variability amplitude and rotation period, which is expected as rotation induces instabilities in the convection zone for the regeneration of magnetic fields through the stellar dynamo.

To understand the different types of stars we classified our catalogue into three classes based on the slope of the convection zone depth. Class III objects ($\geqslant 5400$ K) have very thin convective envelopes and, hence, yield low values of the S_{ph} index. Class II (3900–5400 K) objects show clear signatures of a decrease in the S_{ph} index as T_{eff} increases, i.e., the convective envelope becomes thinner. However, the trend breaks down for Class I ($\leqslant 3900$ K) objects, which show a broad range of magnetic activity. This is possibly owing to the absence of a tachocline and, hence, a turbulent dynamo. The extensive range of stellar activity among all classes might be owing to the presence of a range of stellar ages for all classes. We observed a declining saturated regime in both Class I and II objects at lower Rossby numbers, and the kink is the inflexion point between the saturated and unsaturated regimes. The kink locus we observed is in agreement with that found by Corsaro et al. (2021); See et al. (2021). Instead of a flat, saturated region for lower Rossby numbers (down to $Ro = 0.01$), we observed a minor decline of the saturation limit. This might be caused by bright faculae partially cancelling out dark spots and, hence, reducing the corresponding activity index.

We constructed a chromospheric HR diagram, which tells us that stellar activity decreases for stars hotter than early F-type, owing to the lack of a convective envelope. The activity increases towards K–M-type stars. We found that K-type stars are more magnetically active even than M-type stars. The probable binary systems in our catalogue are the most magnetically active stars. The Sun belongs to a class of low-to-moderately magnetically active stars, and the majority of our sample stars have an S_{ph} index greater than the Sun's. We have not found tightened relationships among stellar magnetic activity, rotation period and/or a number of other stellar parameters. Instead, we have found weak correlations among them, likely because of complex interdependencies. To fully understand these interdependencies, stellar age must be taken into consideration, since it is a key parameter that shows strong connections with both activity and rotation period.

DATA AVAILABILITY

The ZTF data analysed in this paper are publicly available from the Chen et al. (2020) and also from the ZTF Archive. The data underlying this article are available in the article and in its online supplementary material.

REFERENCES

Allard, F., Homeier, D., & Freytag, B. 2011, in Astronomical Society of the Pacific Conference Series, Vol. 448, 16th Cambridge Workshop on Cool Stars, Stellar Systems, and the Sun, ed. C. Johns-Krull, M. K. Browning, & A. A. West, 91

Bailer-Jones, C. A. L., Rybizki, J., Fouesneau, M., Demleitner, M., & Andrae, R. 2021, AJ, 161, 147

Bayo, A., Rodrigo, C., Barrado Y Navascués, D., et al. 2008, A&A, 492, 277

Bopp, B. W., & Fekel, F., J. 1977, AJ, 82, 490

Boro Saikia, S., Marvin, C. J., Jeffers, S. V., et al. 2018, A&A, 616, A108

Caffau, E., Ludwig, H. G., Steffen, M., Freytag, B., & Bonifacio, P. 2011, Sol. Phys., 268, 255

Casagrande, L., & VandenBerg, D. A. 2018, MNRAS, 479, L102

Chen, X., Wang, S., Deng, L., et al. 2020, ApJS, 249, 18

Corsaro, E., Bonanno, A., Mathur, S., et al. 2021, A&A, 652, L2

Cranmer, S. R., & Saar, S. H. 2011, ApJ, 741, 54

Cutri, R. M., Skrutskie, M. F., van Dyk, S., et al. 2003, VizieR Online Data Catalog, II/246

Cutri, R. M., Wright, E. L., Conrow, T., et al. 2021, VizieR Online Data Catalog, II/328

Davenport, J. R. A., & Covey, K. R. 2018, ApJ, 868, 151

de Grijs, R., & Kamath, D. 2021, Universe, 7, 440

Gaia Collaboration, Brown, A. G. A., Vallenari, A., et al. 2021, A&A, 649, A1

Gordon, T. A., Davenport, J. R. A., Angus, R., et al. 2021, ApJ, 913, 70

Green, G. M., Schlafly, E., Zucker, C., Speagle, J. S., & Finkbeiner, D. 2019, ApJ, 887, 93

Hall, J. C. 2008, Living Reviews in Solar Physics, 5, 2

Kubiak, K., Mužić, K., Sousa, I., et al. 2021, A&A, 650, A48

Lanzafame, A. C., Distefano, E., Messina, S., et al. 2018, A&A, 616, A16

Lomb, N. R. 1976, Ap&SS, 39, 447

Mainzer, A., Grav, T., Bauer, J., et al. 2011, ApJ, 743, 156

Masci, F. J., Laher, R. R., Rusholme, B., et al. 2019, Publ. Astron. Soc. Pac., 131, 018003

Mathur, S., Salabert, D., García, R. A., & Ceillier, T. 2014, Journal of Space Weather and Space Climate, 4, A15

McQuillan, A., Mazeh, T., & Aigrain, S. 2014, ApJS, 211, 24

Noyes, R. W., Hartmann, L. W., Baliunas, S. L., Duncan, D. K., & Vaughan, A. H. 1984, ApJ, 279, 763

Parker, E. N. 1955, ApJ, 122, 293

Pecaut, M. J., & Mamajek, E. E. 2013, ApJS, 208, 9

Pizzolato, N., Maggio, A., Micela, G., Sciortino, S., & Ventura, P. 2003, A&A, 397, 147

Reiners, A., Schüssler, M., & Passegger, V. M. 2014, ApJ, 794, 144

Reinhold, T., & Hekker, S. 2020, A&A, 635, A43

Reinhold, T., Reiners, A., & Basri, G. 2013, A&A, 560, A4

Reinhold, T., Shapiro, A. I., Solanki, S. K., et al. 2020, Science, 368, 518

Salabert, D., García, R. A., Beck, P. G., et al. 2016, A&A, 596, A31

Scargle, J. D. 1982, ApJ, 263, 835

See, V., Roquette, J., Amard, L., & Matt, S. P. 2021, ApJ, 912, 127

Skumanich, A. 1972, ApJ, 171, 565

Somers, G., Cao, L., & Pinsonneault, M. H. 2020, ApJ, 891, 29

Stassun, K. G., & Torres, G. 2021, ApJ, 907, L33

Strassmeier, K. G. 2009, A&ARv, 17, 251

van Saders, J. L., & Pinsonneault, M. H. 2012, ApJ, 746, 16

Vaughan, A. H., & Preston, G. W. 1980, Publ. Astron. Soc. Pac., 92, 385

Wang, S., & Chen, X. 2019, ApJ, 877, 116

Wilson, O. C. 1968, ApJ, 153, 221

Wright, E. L., Eisenhardt, P. R. M., Mainzer, A. K., et al. 2010, AJ, 140, 1868

Zhang, J., Zhao, J., Oswalt, T. D., et al. 2019, ApJ, 887, 84

This paper has been typeset from a TEX/LATEX file prepared by the author.